To be cleared for export

For submission to Journal of Geophysical Research

Representation of the geosynchronous plasma environment in spacecraft charging calculations

V. A. Davis and M. J. Mandell, Science Applications International Corporation

M. F. Thomsen, Los Alamos National Laboratory

Abstract

Historically, our ability to predict and "postdict" spacecraft surface charging has been limited by the characterization of the plasma environment. One difficulty lies in the common practice of fitting the plasma data to a Maxwellian or Double Maxwellian distribution function, which may not represent the data well for charging purposes. We use electron and ion flux spectra measured by the Los Alamos National Laboratory (LANL) Magnetospheric Plasma Analyzer (MPA) to examine how the use of different spectral representations of the charged particle environment in computations of spacecraft potentials during magnetospheric substorms affects the accuracy of the results. We calculate the spacecraft potential using both the measured fluxes and several different fits to these fluxes. These measured fluxes have been corrected for the difference between the measured and calculated potential.

The potential computed using the measured fluxes and the best available material properties of graphite carbon, with a secondary electron escape fraction of 81%, is within a factor of three of the measured potential for 87% of the data. Potentials calculated using a Kappa function fit to the incident electron flux distribution function and a Maxwellian function fit to the incident ion flux distribution function agree with measured potentials nearly as well as do potentials calculated using the measured fluxes. Alternative spectral representations gave less accurate estimates of potential. The use of all the components of the net flux, along with spacecraft specific average material properties, gives a better estimate of the spacecraft potential than the high energy flux alone.

1 Background

Spacecraft surface charging has been a topic of investigation for over thirty years [Purvis, *et al.*, 1984; Whipple, 1981; Garrett, 1981a; Davis and Duncan, 1992]. It has been the cause of numerous anomalies on geosynchronous orbiting spacecraft, ranging from annoyances to serious loss of power capability or other functionality [Frezet, *et al.*, 1988; Hoeber, *et al.*, 1998; Koons, *et al.*, 1999]. Engineering practices have evolved to minimize, if not the actual charging itself, at least the most deleterious consequences of charging. A great deal of analytical work has been done to show the relationship between spacecraft geometry, properties of spacecraft surface materials, and the space plasma environment, on the one hand, and the charging of spacecraft, on the other.

Spacecraft surface charging results from the accumulation of charge on spacecraft surfaces. The surfaces of geosynchronous spacecraft can accumulate charge due to incidence of energetic (10 to 50 keV) substorm electrons. The contributions to the current are shown in Figure 1. The balance of the incident electron current with the positive current contributions determines the level of charging. Kilovolt electrons generate secondary electrons and can be backscattered (reflected) from surfaces. Kilovolt ions also generate secondary electrons. Photoemission due to solar ultra-violet generates low energy electrons on sunlit surfaces. The photoemission current density exceeds that of the geosynchronous natural charging currents.

In order to accurately compute surface potentials, spacecraft geometry, surface materials, and environment must all be considered. Each insulating spacecraft surface interacts with the plasma and is capacitively and resistively coupled to the chassis and other surfaces. Electric fields due to differential charging of spacecraft surfaces can trap the secondary and photo electrons. [Whipple, 1976; Mandell, *et al.*, 1978; Olsen, *et al.*, 1981] While the spacecraft chassis might be kilovolts negative, an insulating surface might well be at an either higher or lower potential. The low energy electrons are attracted to surfaces positive with respect to the surface from which they originated and are seen in the lower energy channels (under 200 eV) of particle detectors. The differential potentials that develop between insulating surfaces on the sunlit side and shaded surfaces on the dark side are responsible for most cases of surface charging in sunlight.

Several three-dimensional computer codes are available to compute spacecraft surface charging in a tenuous plasma environment (NASCAP/GEO [Katz, *et al.*, 1979], SEE Interactive

2

Spacecraft Charging Handbook [Katz, *et al.*, 2000], and Nascap-2k [Davis, *et al.*, 2002]). The computer codes all use a Maxwellian or a double Maxwellian distribution function to describe the charging environment. Originally the Maxwellian distribution function was chosen for its simplicity and to our knowledge no one has ever evaluated its adequacy for .computations of potential. In the late 70s and early 80s, when NASCAP/GEO was written, some calculations were done with measured flux spectra. The high noise level and low resolution of the measured flux spectra made the solutions unreliable, which led to the present use of Maxwellian functions. Even though the measured flux spectra available today are far superior to those of the early 80s, analytic functional forms are still generally preferred for charging calculations.

For 12 years, Los Alamos National Laboratory (LANL) has been accumulating high quality measurements of electron and proton energy flux spectra from Magnetospheric Plasma Analyzer (MPA) instruments aboard a series of geosynchronous spacecrafts [Bame *et al.*, 1993]. These data not only provide a plasma characterization but can also be used to infer the potential (relative to plasma) of the instrument ground and the presence of differential charging. At times we have used these data to "postdict" the surface charging of nearby spacecraft, with several successes and a few failures. One difficulty lies in the use of Maxwellian or Double Maxwellian fits to the plasma energy distribution function, which may not represent the data well for surface charging purposes.

Others ([Garrett, *et al.*, 1980], [Lai, *et al.*, 2001], [Mullen, *et al.*, 1986], [Olsen, 1983] and [Thomsen, 2002], among others) have attempted to correlate spacecraft surface charging with simple measures of the electron flux spectra such as the electron temperature moment and the high energy flux. These approaches have met with limited success.

2 Data

The ion and electron flux spectral measurements used in this study were taken by one of a series of Magnetospheric Plasma Analyzer (MPA) instruments built by the Los Alamos National Laboratory (LANL) and flown on a series of geosynchronous spacecraft. Seven instruments are in orbit, one of which has been collecting data since 1989. The MPA is a spherical-sector electrostatic analyzer with a bending angle of 60°. The spin axis of the spacecraft points continuously at the center of the Earth. The MPA is mounted so that the spacecraft spin allows the instrument to view 360 degrees in azimuth. The full angular distribution is measured and

archived. From the full distribution, spin-angle-averaged flux spectra, spacecraft potential, and various moments are computed. LANL maintains a web site that provides spectrograms and moments.

The instrument field of view is divided into six separate but contiguous detectors covering the range of polar angle from about 25° to 155°. The 360 degree azimuthal view is divided into 24 sectors of 15 degrees. Thus in one spin, the MPA views ~92% of a sphere, divided into six polar by 24 azimuthal view directions. The two polar angle detectors, which view nearly perpendicular to the spin axis, give very complete pitch angle coverage. While the spacecraft spins through a 15° azimuthal sector, the MPA plate voltage is swept through 40 logarithmically spaced energy channels ranging from ~40 keV/e down to ~1 eV/e . A complete three-dimensional (40 energies x 24 azimuths x 6 polar angles) distribution is obtained in one 10-s spin. Since the same analyzer is used for ion and electron measurements (by changing the polarity of the plate voltage and channel electron multiplier bias [Bame *et al.*, 1993]), the ion and electron distributions are measured alternately. In 86 s, the instrument cycles through one three-dimensional electron distribution and two three-dimensional ion distributions, as described above, as well as three two-dimensional electron distributions and two high-angular-resolution modes [Bame *et al.*, 1993].

The determination of the spacecraft potential, the moments of the distribution, and the distribution function from the measurements are described in the following publications: [Lawrence, *et al.*, 1999], [McComas, *et al.*, 1993], [Thomsen, *et al.*, 1996], [Thomsen, *et al.*, 1999]. Simplified descriptions of some of this processing are included in the body of this paper in order to explain how the measurements are being used here.

From the data archived at LANL, we constructed a dataset of measurements made in eclipse by the spacecraft 1994-084 during September 2001 for which the ion flux spectrum provides a distinct ion line to determine the potential and the data quality flags are acceptable. This study used only eclipse data to eliminate the variation in escaping photocurrent due to variations in sun angle on the geometrically complex spacecraft. The dataset has 973 records. Each record includes a spin-averaged ion flux spectrum, a spin-averaged electron flux spectrum, and the measured potential.

3 Electron and ion flux spectra

3.1 Flux spectrum observed by a charged spacecraft

Figure 2 and Figure 3 show the ion flux spectrum and the electron flux spectrum for the same time. The data points labeled "Flux at spacecraft" are the spin-averaged, measured fluxes. The data points labeled "One-count" are the average fluxes that would be measured if one particle hit one of the six detectors. This is an approximate value as the six detectors have different geometric factors and efficiencies. For this work, we treat flux values under twice the one-count rate as zero or unknown, depending on the context.

The energy channel in which the ion count rate increases dramatically gives the spacecraft potential. In Figure 2 the lowest energy channel with a significant count rate is 2450 to 3200 eV. The chassis potential is taken to be the geometric mean of the energy channel edges, -2800 V. An ion with nearly zero energy at infinity is accelerated to 2800 eV by the time it reaches the detector, which is why no ions are seen below the 2450 to 3200 eV energy channel.

The negatively charged spacecraft repels electrons. An electron with energy of 2800 eV at infinity reaches the detector with zero energy, and lower energy electrons do not reach the detector at all. However, electrons are seen by the detector with energies of less than 30 eV (and on highly charged spacecraft, sometimes even 200 eV). These secondary electrons are generated on the spacecraft surface or in the spacecraft vicinity and are trapped by electric fields due to differential charging.

The accuracy of a spacecraft potential measurement is the width of the energy channel, approximately 30% of the energy. The accuracy of the energy of each flux measurement can be estimated to be on the order of half the width of the energy channel in which the measurement is made plus half the width of the energy channel of the ion line. The accuracy of the flux is given by Poisson statistics to be the geometric mean of the measured spin-averaged flux and the one-count flux.

3.2 Adjusting flux spectra to account for chassis potential

The ambient fluxes can be determined from the fluxes measured at the spacecraft. The relation is derived from a consideration of the distribution function. The differential flux as a function of energy is related to the phase space distribution function by the expression

$$f(E) = \left(\frac{m^2}{2Ee^2}\right) F(E) \tag{1}$$

where f is the distribution function in $s^3 m^{-6}$, F is the measured differential flux in $(m^2 \text{ s sr eV})^{-1}$, E is the particle energy in eV, e is the charge on the electron in Coulombs, and m is the mass of the species in kg. The measured energy is shifted from the energy at infinity by the potential: $E_m = E_\infty \mp \phi$, where the "-" sign is for ions and the "+" sign is for electrons.

Liouville's theorem states that "the density of systems in the neighborhood of some given system in phase space remains constant in time." [Goldstein, 1950a] Krall and Trivelpiece [1986] state Liouville's theorem as "f(**x**, **v**, t) is constant along any particle trajectory." For our purposes, we can state Liouville's theorem as "if all possible particle trajectories that begin at the spacecraft end at infinity, the distribution function at the spacecraft is the same as the distribution function at infinity." If we treat the spacecraft as a uniform sphere, the potential varies only radially. All particles in an attractive, radially-symmetric potential field that varies more slowly than the inverse distance square have trajectories that connect to infinity. If the potential field varies faster than the inverse distance squared, some particle trajectories both begin and end on the sphere due to angular momentum considerations [Goldstein, 1950b]. In a repulsive, radially-symmetric potential field (such as electrons near a negative potential sphere), all particle trajectories connect to infinity.

As the value of the distribution function at the spacecraft is the same as the value of the distribution function at infinity, we have that

$$f_\infty(E_\infty) = f_m(E_m)$$
$$\frac{m^2}{2E_\infty} F_\infty(E_\infty) = \frac{m^2}{2E_m} F_m(E_m) \tag{2}$$
$$F_\infty(E_m \pm \phi) = F_m(E_m)\left(1 \pm \frac{\phi}{E_m}\right)$$

6

where the "+" sign is for ions and the "-" sign is for electrons.

Figure 2 and Figure 3 show the flux spectra shifted to infinity. The ion flux spectrum is fairly flat. The lower energy electrons, which were generated at the spacecraft surface, are concentrated just above the spacecraft potential. These electrons must be excluded from the "ambient" flux.

3.3 Flux spectrum measured by an uncharged spacecraft

Figure 4 shows electron and ion flux spectra for a nearly uncharged spacecraft (-5.4 V). The flux spectra are definitely not Maxwellian. There is a low energy (about 7 eV) peak for both species. That the peak appears in both flux spectra, rather than just the ion flux spectra, suggests that the spacecraft is actually uncharged and that the ion and electron flux spectra are superpositions of two different populations: a 7 eV population (of plasmaspheric origin) and a multi-kilovolt population. The electron flux spectrum is very broad and steadily decreasing with energy. The multi-kilovolt portion of the ion flux spectrum is approximately flat to the highest energies measured.

4 Moments

To gain some general insight into the flux spectra, we calculate the density and temperature moments. These are given by

$$n_{(e,i)} = \frac{4\pi e}{m}\sqrt{\frac{2e}{m}}\int_0^\infty f(E_\infty)\sqrt{E_\infty}\,dE_\infty = 2\pi\sqrt{\frac{2m}{e}}\sum_{E>E_{min}}\frac{F(E)}{E}\sqrt{E-\phi_m}\,\Delta E \qquad (3)$$

$$\theta_{(e,i)} = \frac{2}{3en}\pi m\left(\frac{2e}{m}\right)^{5/2}\int_0^\infty f(E_\infty)\sqrt{E_\infty}^3\,dE_\infty = 2\pi\frac{2}{3n}\sqrt{\frac{2m}{e}}\sum_{E>E_{min}}\frac{F(E)}{E}(E-\phi_m)^{3/2}\,\Delta E \qquad (4)$$

Where F is the measured differential flux, E_∞ is the energy at infinity, E is the geometric mean of the edges of the energy channel, ΔE is the width of the energy channel, and ϕ_m is the measured chassis potential. The value used for E_{min} for electrons is 30 eV. The value of E_{min} for ions is zero. The minimum for electrons is chosen to filter out the secondary and photoelectrons accelerated by local electric fields into the MPA.

The average values and the standard deviations of the density and temperature moments are given in Table 1. Figure 5 through Figure 8 show the relationships between these moments.

As seen in Figure 5, when the electron temperature moment is viewed as a function of electron density moment, the measurements sort into two populations. The flux spectra with higher values of the temperature moment may be from fresh night-side plasma sheet particles that have been accelerated by substorm electric fields and the flux spectra with a lower temperature moment may be dominated by upwelling plasma. The temperature-density relation of the low temperature moment population can be well fit by a power law. The temperature moment varies inversely with the 0.70 power of the density moment. This relationship is similar to those observed by Garrett *et al.*, [1981b] between energy density and number density and between energy flux and number flux. This relationship does not apply to the measurements with a higher temperature moment. Open triangles are used to distinguish the measurements with a lower electron temperature moment in this and subsequent figures.

The ion temperature moment versus density moment curve is shown in Figure 6. The power law that best fits these points is $\theta_i \sim n_i^{-1.07}$.

If we exclude the low temperature measurements, the ion and electron density moments shown in Figure 7 are correlated and comparable. This is consistent with the fact that we expect the plasma to be neutral on a length scale of the order of the Debye length (hundreds of meters). The low energy cutoff in the moment integral may be excluding a significant contribution to the density from low energy electrons in the low temperature measurements. The ion and electron temperature moments shown in Figure 8 are also correlated and comparable. Ion temperature moments are generally higher than electron temperature moments.

[Thomsen, 2001] reports a power law relationship between an electron temperature moment and the spacecraft chassis potential. For this relationship, an additional term is added to the electron temperature moment to account for the cold electron population. The electron temperature moment of the spectrum below 30 eV is assumed to be approximately 5 eV and the cold electron density is represented by the cold ion density.

$$\langle \theta \rangle = \frac{n_{lp} \times 5\,eV + n_e \times \theta_e}{n_{lp} + n_e} \tag{5}$$

where n_e and θ_e are computed from Equations (3) and (4) using E_{min} of 30 eV, and n_{lp} is computed from Equation (3) where the sum is over the energy channels *under* 124 eV. Separate power law fits were developed for eclipse and sunlit conditions. For eclipse

$$\phi = 1.74 \times 10^{-5} \langle \theta \rangle^{2.26} \tag{6}$$

In addition, no charging in excess of -20 V is observed unless the electron energy density exceeds about 900 eV cm^{-3}. Figure 9 shows this relationship for this dataset. The fit, shown by the line in the figure, is consistent with this dataset. The magnitude of the potential of all the low energy electron population data points, shown with open triangles, is under 18 V and is independent of the averaged temperature moment. These spectra have an electron energy density under 250 eV cm^{-3}.

5 Net Fluxes

The balance of the net electron flux and net ion flux determines the spacecraft floating potential. The incident fluxes depend only on the environment and are measured by the MPA. However, the secondary and backscattered electron fluxes depend on the spacecraft materials and geometry. In the absence of geometric and surface material information about this spacecraft, we model it as a sphere of a single surface material at the chassis potential. To account for the trapping of low-energy secondary electrons, we include a factor γ, the fraction of secondary electrons that escape, in our flux expression. The computation of fluxes requires knowledge of the average yield properties of the spacecraft surfaces. The properties we use for the calculations described here are those of graphite. The electron-generated secondary yield properties are chosen to fit the curve in Barnett, *et al.* [1977], which tabulates data from Holzland and Jacobi [1969] and Bruining [1938]. The ion-generated secondary yield properties are chosen to be consistent with the curve for incident Hydrogen ions in Barnett, *et al.* [1977], which tabulates data from Large and Whitlock [1962]. The effective atomic number, which is used to compute the backscatter, is the default value for graphite in the SEE Interactive Spacecraft Charging Handbook [Katz, *et al.*, 2000].

We define the net electron flux to the spacecraft as the incident electron flux minus the sum of the secondary electron flux and the backscattered electron flux. We write this as

$$\text{Flux}_{net}^e = \int_0^\infty F_e(E)\big[1-\gamma Y_e(E)-B(E)\big]dE = \sum_{E>E_{min}} F_e(E)\big(1-\gamma Y_e(E)-B(E)\big)\Delta E \qquad (7)$$

where the Ys and B are the secondary and backscatter yield functions. For the lower energy limit of the electron flux integrals, E_{min}, we use the maximum of $-\phi_m/2$ and 30 eV. This eliminates the bulk of the secondary electrons, while including some of the structure in the low energy portion of the electron flux spectrum. Figure 10 shows the measured chassis potential as a function of the incident and net electron fluxes, computed assuming that all the secondary electrons escape from the spacecraft ($\gamma=1$). At the higher potentials, the measured incident electron flux goes down as the spacecraft potential goes up in magnitude becausethe spacecraft potential attenuates a larger fraction of the incident flux. The net electron flux shows a weak dependence on potential.

Figure 11 shows the chassis potential as a function of the incident and net ion flux to the spacecraft. The ion sum is over all energies for which the ion flux exceeds twice the one-count flux.

$$\text{Flux}_{net}^i = \int_{-\phi}^\infty F_i(E)\big[1+\gamma Y_i(E)\big]dE = \sum_E F_i(E)\big(1+\gamma Y_i(E)\big)\Delta E \qquad (8)$$

Figure 10 and Figure 11 illustrate the difficulty of assuming that the potential is a function of any one of the incident electron flux, the net electron flux, the incident ion flux, or the net ion flux. While for potential magnitudes over 20 V, the average net electron flux becomes more negative with increasing potential magnitude, the net electron flux value does not provide a good prediction of the potential.

The net charging flux to the spacecraft, shown in Figure 12, is the net ion flux minus the net electron flux. When the net charging flux is negative, the spacecraft is charging negative, and when the net charging flux is positive, the spacecraft is charging positively. At steady state, the net charging flux is zero. (In sunlight, the photocurrent also contributes to the net charging flux.) If we have a perfect measurement of the flux spectrum, perfect knowledge of the material properties (secondary and backscatter yields), and there are no geometric effects, the computed net charging flux would be zero at the floating potential. Figure 12 shows a small positive net charging flux with a large amount of scatter for the entire range of floating potentials. Comparing

Figure 10, Figure 11, and Figure 12, the computed net charging flux is on the order of 10% of the incident electron flux and comparable to the incident ion flux. Such a large computed net charging flux indicates the need for improved yield functions and/or calculational techniques.

Net charging flux calculations were also done using material property sets appropriate to optical solar reflectors, solar cells, Gold, and Kapton taken from the SEE Interactive Spacecraft Charging Handbook [Katz, *et al.*, 2000]. These sets of material properties each give a much larger positive net charging flux than does graphite for spacecraft potentials in the hundreds to thousands of volts. Therefore, we continue to use graphite material properties.

6 Chassis potential computation

Our motivation for this work is the desire to predict and postdict spacecraft surface potentials for a given spacecraft from available geometric, material, and magnetospheric environment information. We use the MPA dataset to evaluate characterizations of the environment for these calculations as it provides measurements of the incident ion and electron fluxes and the resulting spacecraft potential. To evaluate the quality of an environment description for potential computation, we compare the measured potential with the calculated potential obtained as follows:

1. We use Equation (2) to estimate the flux spectra at infinity from the ion and electron flux spectra and the measured potential.

2. Using these ion and electron flux spectra at infinity, we determine the net charging flux (incident, secondaries, and backscattered) to the spacecraft as a function of an assumed chassis potential.

3. We search for a unique chassis potential at which the net charging flux is zero. This is the computed chassis potential.

If a potential can be computed and if the measured and computed potentials are the same within the experimental error, the flux spectra and the simplifying assumptions used to compute the net charging flux are considered adequate to compute the chassis potential. Section 3.2 above addresses step one, Section 6.1 below addresses step two, and Section 6.2 addresses step three.

6.1 Net charging flux

In eclipse, the net current to a spacecraft is given by the incident electron current minus the sum of the electron-induced secondary electron current, the backscattered electron current, the incident ion current, and the ion-induced secondary electron current.

$$I_{net} = -I_e + I_{ese} + I_{be} + I_i + I_{ise} \tag{9}$$

Written in terms of measured fluxes at the spacecraft we have

$$F_{net} = \int_{-\phi}^{\infty} F_i(E)\left[1 + \gamma Y_i(E)\right]dE - \int_0^{\infty} F_e(E)\left[1 - \gamma Y_e(E) - B(E)\right]dE$$

where F_{net} is the net charging flux to the spacecraft and γ is the fraction of secondary electrons that escape. Using the formulas in Section 3.2, the net charging flux at a different potential, ϕ', is given by

$$F_{net}(\phi') = \int_{-\phi_m}^{\infty} dE_m \left(1 + \frac{\phi_m - \phi'}{E_m}\right) F_i(E_m)\left[1 + \gamma(\phi')Y_i(E_m + \phi_m - \phi')\right]$$

$$- \int_{max(0,\phi_m-\phi')}^{\infty} dE_m \left(1 - \frac{\phi_m - \phi'}{E_m}\right) F_e(E_m)\left[1 - \gamma(\phi')Y_e(E_m - \phi_m + \phi') - B(E_m - \phi_m + \phi')\right] \tag{10}$$

The electron integral is only strictly correct if the computed potential is more negative than the measured potential, $\phi' < \phi_m$. While the portion of the electron flux spectrum that is not measured because it does not have enough energy to reach the spacecraft should be included in the integral, for the purposes of these calculations, it is assumed to be small.

When using measured fluxes, the integral becomes a sum with the value of E_m taken to be the energy at the geometric center of the energy channel. Contributions to the ion integral in which the measured flux is less than twice the one-count flux are ignored. Contributions to the electron integral in which $E_m < E_{min}$ are discarded, as the flux measurement is dominated by secondary electrons. For both the ion and electron integrals, the lowest energy channel included is the one for which the E_m value exceeds the lower limit of the integral, which results in an overestimate half of the time and an underestimate the other half.

12

6.2 Minimum in net charging flux

The potential range from -1 V to -10,000 V is searched for a potential at which the computed net charging flux is zero. At times there is no zero in the computed net charging flux between -1 V and -10,000 V. In these cases, the potential for which the net charging flux is a minimum is used. Figure 13 shows the resulting estimated potentials. The calculated potential is with a factor of 1.5 of the measured potential for 45% of the data points; the calculated potential is within a factor of 3 of the measured potential for 69% of the data points; and 17% of the data points do not have a solution.

6.3 Error bars

The measured potential has a sizeable error bar, which results in corresponding error bars in the net charging flux calculations. Throughout most of the energy range of the MPA instrument, the energy of the upper edge of the energy channel is approximately 1.31 times the energy of the lower edge. The measured potential is the geometric center of the lowest energy channel with a significant number of counts. (The actual algorithm is much more complex than this [Thomsen, *et al.*, 1999], but for present purposes this simplification is adequate.) Therefore, the actual potential is only measured within a factor of 1.15:: $\phi/1.15 < \phi_{actual} < 1.15\phi$. The use of the measured potential to estimate the ambient fluxes at infinity thus introduces possible error into the computation of the net charging flux. Treating the spacecraft as a uniform sphere introduces further error.

6.4 Dependence on lower energy limit in sum

Another aspect of the integral to be considered is the lower energy cutoff in the electron flux spectrum. When the spacecraft is charged, the low energy part of the electron flux spectrum is usually dominated by low energy secondary electrons trapped by differential potentials near the detector. The lower limit of the electron integrals needs to be as low as possible while high enough to eliminate the trapped electrons. Alternative estimates of this limit gave either similar or less accurate results than the maximum of $-\phi/2$ and 30 eV used here.

13

6.5 Fraction of low energy electrons escaping

An important factor that is not included in the above flux calculations is that not all secondary electrons escape the spacecraft. (Backscattered electrons have higher energies and are unlikely to be trapped.) Rewriting Equation (10), the net charging flux, which on the timescale of MPA measurements is always equal to zero, is given by

$$F_{net} = 0 = -F_e + F_i + F_{back} + \gamma F_{sec} \tag{11}$$

where F_{sec} is secondaries from both ions and electrons and γ is the fraction of secondary electrons that escape.

For each energy, we then have an expression for γ in terms of quantities that we have been calculating:

$$\gamma = \frac{F_e - F_i - F_{back}}{F_{sec}} \tag{12}$$

The low energy flux to the MPA, which we have been carefully keeping out of our flux integrals, consists of low energy electrons that do not escape. The fraction of the created low energy flux that returns to the spacecraft and is measured by the MPA is given by

$$\beta = \frac{\text{measured low energy flux}}{F_{sec}} \tag{13}$$

If the MPA happens to be located at an "average" point on the spacecraft, $\gamma + \beta \sim 1$. The average value of $\gamma + \beta$ computed in this way for this data set is 0.95, slightly under 1.0. Therefore, the measured low energy flux is a useful representation of the average low-energy return flux. The average value of γ for measurements with a chassis potential over 16 V is 0.81.

If we assume that only 81% of the secondary electrons escape, the net fluxes look as shown in Figure 14. The calculated net charging flux approaches zero over the entire range of floating potential. The corresponding estimated potential is shown in Figure 15. 66% of the points have a solution within a factor of 1.5 of the measured potential; 87% of the points have a solution within a factor of 3 of the measured potential; and only 8% do not have a solution. Almost all of the points for which no solution can be found have a potential below 30 V. This is significantly better than the results obtained assuming that all low energy electrons escape, shown in Figure 13.

14

6.6 Alternative predictors

In evaluating this approach to predicting potential from the measured flux spectra, we need to compare this approach with others. Figure 16 shows the potentials predicted by the correlation previously observed between the electron temperature moment and the spacecraft chassis potential. The relationship only applies if the energy density is above a threshold value. This approach always provides a potential estimate. The predicted potential is within a factor of 1.5 of the measured potential for 57% of the points and within a factor of 3 for 70% of the points. It does not work when the measured potential is below about 20 V. This relationship is *not* as good a predictor as current balance using the full flux spectrum.

Several authors [Garrett, *et al.*, 1980; Mullen *et al.*, 1986; Olsen, 1983] have found a relationship between the incident electron flux in the higher energy channels and the potential. We examined single energy channels and all energy channels above a specific energy as possible predictors of the potential for this dataset. The best predictor for this dataset is the sum of the energy channels from 9123 V and above. The fit is

$$\phi_{estimated} = 1.359 \times 10^{-12} \sum_{E>9123} \left(F_e(E) \Delta E \right)^{2.03} \tag{14}$$

This approach always provides a potential estimate. The result is shown in Figure 17. The potential predictions are best at the highest potentials. However, for this dataset it provides less accurate potentials than either current balance using the full flux spectrum or the electron temperature moment. This may be because the highest energy channel for this data is at lower energies than in the papers cited above.

7 Fitting techniques and results

The use of analytic fits to measured incident fluxes is generally preferred to the use of measured fluxes directly in spacecraft surface charging calculations. Calculations using analytic expressions for the incident fluxes are much less likely to be numerically unstable or to give unphysical results. Analytic expressions are also more easily generalized when relevant measurements are not available.

Spacecraft potentials were calculated from fits to measured fluxes using three different functional forms. These computed potentials are then compared with the measured potentials.

15

$$\text{Flux}^{\text{Maxwellian}}(E) = en \sqrt{\frac{1}{2\pi me\theta}} \frac{E}{\theta} \exp\left(-\frac{E}{\theta}\right) \tag{15}$$

$$\text{Flux}^{\text{DoubleMaxwellian}}(E) = en_1 \sqrt{\frac{1}{2\pi me\theta_1}} \frac{E}{\theta_1} \exp\left(-\frac{E}{\theta_1}\right) + en_2 \sqrt{\frac{1}{2\pi me\theta_2}} \frac{E}{\theta_2} \exp\left(-\frac{E}{\theta_2}\right) \tag{16}$$

$$\text{Flux}^{\text{Kappa}}(E) = A E \left(1 + \frac{E}{\kappa E_o}\right)^{-\kappa-1} \tag{17}$$

The θ, n, κ, E_o, and A values are fitting parameters. The Kappa function has the shape of a Maxwellian at low energies and a power law at high energies, providing a high-energy tail to the distribution. The Kappa distribution was selected because Christon, *et al.* [1989] have shown that it provides a good fit to the quiescent plasma sheet environment at greater than 12 R_E. (Geosynchronous is at 6.6 R_E.) The active magnetosphere is more complex [Christon, *et al.*, 1991]. We are looking for a simple model of the environment appropriate for use in calculations, so we explore the use of a single Kappa distribution. We also did calculations using fits to quadratic, exponential, and power law distributions. The potentials computed using these functional forms generally do not agree with the measured potentials and are not discussed here.

The proposed functional forms are appropriate for the flux at infinity. Before fitting the measured fluxes to a functional form, the measured fluxes are adjusted for the measured potentials using Equation (2).

Two least-squares fitting procedures were used. The Maxwellian function is fit by taking logarithms of the flux and the energy and computing the best-fit straight line. Each point is weighted by the energy channel width. The fitting procedure ("lfit" from *Numerical Recipes* [Press, *et al.* 1992]) finds values for a and b that minimize the expression

$$\sum_i \left(\Delta_i \left(y_i - a - bx_i\right)\right)^2 \tag{18}$$

where

$$\Delta_i = \Delta E$$

$$y_i = \ln F_\infty - \ln E$$

$$x_i = E$$

The Double Maxwellian and Kappa functions are fit using the Levenberg-Marquardt method for nonlinear least-squares fitting. The algorithm and an implementation in C are described in *Numerical Recipes* [Press, *et al.* 1992]. Again the points are weighted by the energy channel width. The fitting procedure finds the vector **a** that minimizes the expression

$$\sum_i \left(\Delta_i \left(y_i - f(\mathbf{a}, x_i) \right) \right)^2 \tag{19}$$

where

$\Delta_i =$ ΔE

$y_i =$ F_∞

$x_i =$ E

$f =$ Functional form

$\mathbf{a} =$ Vector of the constants in the functional form. For a Kappa distribution, $\mathbf{a} = (A, E_o, \kappa)$. For a double Maxwellian distribution, $\mathbf{a} = (n_1, \theta_1, n_2/n_1, \theta_2/\theta_1)$.

We also used the second approach to fit the flux distribution to a Maxwellian. The results are not meaningfully different than those obtained using the first (simpler) fitting approach.

In fitting ion flux spectra, the portion of the flux spectrum fit is from the highest energy channel through the energy channel just above the potential, excluding energy channels in which the flux is below twice the one-count equivalent flux. In fitting electron flux spectra, the portion of the flux spectrum fit is the range over which the flux integrals are done. This avoids all energy channels with possibly misleading count rates.

Fluxes can be computed from fit distributions in exactly the same way as they are computed from the measured distributions. With fit distributions, it is possible to include energy channels that are not included in the integrals over the measured distribution, such as ion fluxes below twice the one-count flux equivalent, electron energy channels below the estimated potential barrier, and energy channels above the maximum of the instrument, 47 keV. The maximum energy chosen can affect the results a great deal, particularly for the ions. The extension of the fit to higher energies generally contributes a large net ion flux to the current balance. We use an upper limit for the net flux integrals of about 100 keV.

Potentials can be computed from the fit fluxes. Table 2 summarizes the accuracy of computed potentials using the various combinations of distribution function analytic forms. The average error is given by

$$\text{Average error} = \sqrt{\sum \left(\left(\frac{\phi' - \phi}{\phi} \right)^2 \right)} \qquad (20)$$

where the sum is over those data points for which a computed potential can be found. The potentials computed using Maxwellian fits for both ions and electrons are within a factor of 1.5 of the measured potential for 39% of the data and within a factor of 3 of the measured potential for 62% of the data. Using a Kappa distribution for the electrons and a Maxwellian distribution for the ions gave results within a factor of 1.5 of the measured potential for 65% of the data and within a factor of 3 of the measured potential for 80% of the data. Potential predictions using the electron Kappa-ion Maxwellian fit combination give results similar to those obtained from using the measured fluxes directly.

Figure 18 shows the measured potential as a function of the potential computed from the fits to the fluxes for the most successful fit, a Maxwellian for the ions and a Kappa function for the electrons. Figure 19 and Figure 20 show how the quality of the prediction degrades if the same functional form is used for both species. In Figure 18, there are a handful of points in the lower right hand corner. These points have measured potentials under 10 V and computed potentials on the order of a few hundred volts. For several of these cases, the temperature moment for the Maxwellian fit to the ion flux spectrum is of the order of a thousand and there is a peak in the measured flux spectrum around 10 V. Upon careful examination of the flux spectra, which are similar to that shown in Figure 1, we concluded that the fitting procedure provides a good fit to the higher energy portion of the flux spectrum where there are far more data points and a poor fit to the lower energy portion of the spectrum. The fits would provide more accurate potential calculations if the fitting procedure were modified to fit the lower energy portion of the spectrum when a peak exists in that region.

Table 3 compares the accuracy of potentials computed from fits in which the flux integrals include all the energy channels and extend up to 100 keV with the accuracy of potentials computed from fits in which the flux integrals include only those energy channels used in

calculating the fit. Neither approach provides more consistently accurate computations of potential than the other.

8 Summary and Discussion

The LANL dataset has proven to be a powerful tool for the investigation of spacecraft surface charging. The flux spectra provide the resolution and accuracy needed for "postdiction" spacecraft surface charging calculations.

Using the measured flux spectra, we determined that, for this spacecraft, computing the fluxes using a set of material properties for graphite carbon and a low-energy secondary electron escape fraction of 81% gives computed potentials consistent with measured values. The estimated potential is within a factor of 1.5 of the measured potential for 66% of the data and within a factor of 3 of the measured potential for 87% of the data. While this approach is valid for any spacecraft in eclipse, where geometric effects are less important, we expect that the specific material properties and secondary electron escape fraction are spacecraft specific quantities.

It is necessary to include all the current components—incident electrons and ions, secondary electrons, backscattered electrons, and photoelectrons—to accurately postdict chassis potentials from measured flux spectra. This approach provides a better prediction of chassis potentials than either the measured temperature moment or the integrated measured flux between 9 and 47 keV.

Potential "postdictions" using a Kappa distribution to fit the incident electron flux spectrum and a Maxwellian distribution to fit the incident ion flux spectrum give results similar to "postdictions" using the measured flux spectra directly. We expect better results would be obtained if additional intelligence in the low energy portion of the flux spectrum were added to the ion flux fitting procedure. While the material properties and secondary electron escape fraction are spacecraft-specific, the conclusion regarding the best functional forms to use for the environment does not depend on the specific spacecraft studied.

The difference between a Maxwellian distribution and a Kappa distribution is in the tail of the distribution. The Kappa distribution falls off more slowly with energy. The difference between the accuracy of results computed using the two types of fits is consistent with earlier work by Katz et al. [1986] in which it was shown that the form of the secondary yield in the 5 to 50 keV energy range is critical to the computation of spacecraft surface charging.

19

While this study has established that a Kappa distribution is preferred to a Maxwellian distribution to fit an observed electron flux spectrum, the question of the appropriate parameters to use for preflight predictions remains. In addition, a similar study using sunlit data and spacecraft geometric information would eliminate the uncertainty introduced by the use of a self-consistently determined average secondary electron escape fraction and confirm that the Kappa distribution is appropriate at all local times.

9   Acknowledgements

10 References

S.J. Bame, D.J. McComas, M.F. Thomsen, B.L. Barraclough, R.C. Elphic, J.P. Glore, and J.T. Gosling, Magnetospheric plasma analyzer for spacecraft with constrained resources, *Rev Sci Instrum 64*, p 1026, 1993.

C.F. Barnett, J.A. Ray, E. Ricci, M.I. Wilker, E.W. McDaniel, E.W. Thomas, H.B. Gilbody, *Atomic data for controlled fusion research,* Oak Ridge National Laboratory, Tennessee, (ORNL-5207, 1977.

H. Bruining, Philips, *Technical Review. 3*, p. 80, 1938.

W.Y. Chang, J.R. Dennison, Neal Nickles and R.E. Davies, "Utah State University ground-based test facility for study of electronic properties of spacecraft materials," *Proceedings of the 6th Spacecraft Charging Technology Conference*, AFRL-VS-TR20001578, 2000.

S.P. Christon, D.J. Williams, and D.G. Mitchell, L.A. Frank, C.Y. Huang, Spectral characteristics of plasma sheet ion and electron populations during undisturbed geomagnetic conditions, *J. Geophys. Res. 94,* A10, p 13,409, 1989.

S.P. Christon, D.J. Williams, and D.G. Mitchell, C.Y. Huang, L.A. Frank, Spectral characteristics of plasma sheet ion and electron populations during disturbed geomagnetic conditions, *J. Geophys. Res. 96,* A1, p 1, 1991.

V.A. Davis and L.W. Duncan, *Spacecraft Surface Charging Handbook*, Air Force Report PL-TR-92-2232, November 1992.

V.A. Davis, L.F. Neergaard, M.J. Mandell, I. Katz, B.M. Gardner, J.M. Hilton, J. Minor, Spacecraft charging calculations: Nascap-2K and SEE Spacecraft Charging Handbook, *40th AIAA Aerospace Sciences Meeting and Exhibit*, AIAA 2002-0626, 2002.

B. Feuerbacher and B. Fitton, Experimental Investigation of Photoemission from Spacecraft Surface Materials, *J. Appl. Phys. 43*, 1563, 1972.

M. Frezet, J.P. Granger, L. Levy, and J. Hamelin, "Assessment of charging behaviour of Meteosat spacecraft in geosynchronous environment," ONERA Paper 233-248, presented at CERT, 4th International Conference on Spacecraft Materials in Space Environment, Toulouse, France, September 1988.

H.B. Garrett, The Charging of Spacecraft Surfaces, *Reviews of Geophysics and Space Physics, 19*, 4, p. 577, 1981a.

H.B. Garrett, A statistical analysis of the low-energy geosynchronous plasma environment-I. Electrons, *Planet. Space Sci. 29*, 10, p. 1021, 1981b.

H.B. Garrett, D.C. Schwank, P.R. Higbie, D.N. Baker, Comparison between the 30 to 80 keV electron channels on ATS 6 and 1976-059A during conjunction and application to spacecraft charging prediction, *JGR 85*, p 1155, 1980

H. Goldstein, *Classical Mechanics*, Addison-Wesley Publishing Company, Inc. Massachusetts, p. 267, 1950a.

H. Goldstein, *Classical Mechanics*, Addison-Wesley Publishing Company, Inc. Massachusetts, p. 67-68, 1950b.

C.F. Hoeber, E.A. Robertson, I. Katz, V.A. Davis, and D.B. Snyder, "Solar array augmented electrostatic discharge in GEO," AIAA Paper 98-1401, presented at AIAA, *International Communications Spacecraft Systems Conference and Exhibit*, 17th, Yokohama, Japan, February 1998.

J. Holzl and K. Jacobi, *Surface Science, 14*, p 351, 1969.

I. Katz, J.J. Cassidy, M.J. Mandell, G.W. Schnuelle, P.G. Steen, J.C. Roche, The capabilities of the NASA Charging Analyzer Program, *Spacecraft Charging Technology-1978,* NASA CP-2071, AFGL-TR-79-0082, edited by R.C. Fincke and C.P. Pike, P. 101, 1979.

I. Katz, M.J. Mandell, G.A. Jongeward, The importance of accurate secondary electron yields in modeling spacecraft charging, *JGR, 91,* A12, p. 13739, 1986.

I. Katz, V.A. Davis, M.J. Mandell, B.M. Gardner, J.M. Hilton, J. Minor, A.R. Fredrickson, D.L. Cooke, Interactive spacecraft charging handbook with integrated updated spacecraft charging models, *38th Aerospace Sciences Meeting and Exhibit,* AIAA 2000-0247, 2000.

H.C. Koons, J.E. Mazur, R.S. Selesnick, J.B. Blake, J.F. Fennell, J.L. Roeder, and P.C. Anderson, *The Impact of the Space Environment on Space Systems,* Aerospace Report TR-99 (1670)-1, The Aerospace Corporation, 1999.

N. A. Krall and A. W. Trivelpiece, *Principles of Plasma Physics,* San Francisco Press, Inc., California, p. 447, 1986.

S.T. Lai, D. J. Della-Rose, Spacecraft charging at geosynchronous altitudes: new evidence of existence of critical temperature, *J Spacecr 38,* p. 922, 2001

L. N. Large and W. S. Whitlock, Secondary electron emission from clean metal surfaces bombarded by fast hydrogen ions, *Proceedings of the Physical Society 79,* p 148, 1962.

D.J. Lawrence, M.F. Thomsen, J.E. Borovsky, and D.J. McComas, Measurements of early and late-time plasmasphere refilling, *JGR, 104,* p 14691, 1999

M.J. Mandell, I. Katz, G.W. Schnelle, P.G. Steen, J.C. Roche, The decrease in effective photocurrents due to saddle points in electrostatic potentials near differentially charged spacecraft, *IEEE Trans. Nucl. Sci., NS-25,* 6, p. 1313, 1978.

D.J. McComas, S.J. Bame, B.L. Barraclough, J.R. Donart, R.C. Elpheric, J.T. Gosling, M.B. Moldwin, K.R. Moore, and M.F. Thomsen, Magnetospheric plasma analyzer: initial three-spacecraft observations from geosynchronous orbit, *JGR, 98,* A8, p 13453, 1993.

E.G. Mullen, M.S. Gussenhoven, D.A. Hardy, T.A. Aggson, B.G. Ledley, E. Whipple, SCATHA survey of high-level spacecraft charging in sunlight, *J. Geophys. Res, 91,* A2, p. 1474, 1986.

N. Nickles, R.E. Davies and J.R. Dennison, "Applications of secondary electron energy- and angular-distributions to spacecraft charging," *Proceedings of the 6th Spacecraft Charging Technology Conference*, AFRL-VS-TR20001578, 2000.

R.C. Olsen, C.E. McIlwain, E.C. Whipple, Jr., Observations of differential charging effects on ATS 6, *JGR, 86,* A8, p. 6809, 1981.

R.C. Olsen, A threshold effect for spacecraft charging, *J. Geophys. Res., 88*, A1, 493, 1983.

W. H. Press, S. A. Teukolski, W. T. Vetterling, B. P. Flannery, *Numerical Recipes in C, The Art of Scientific Computing*, 2nd Edition, Cambridge University Press, 1992.

Purvis, C.K., H.B. Garrett, A.C. Whittlesey, and N.J. Stevens, *Design Guidelines for Assessing and Controlling Spacecraft Charging Effects*, NASA Technical Report Paper 2361, September 1984.

M. F. Thomsen, D. J. McComas, G.D. Reeves, and L.A. Weiss, An observational test of the Tsyganenko (T89a) model of the magnetospheric field, *JGR 101*, A11, p. 24827, 1996.

M.F. Thomsen, E. Noveroske, J.E. Borovsky, D.J. McComas, *Calculation of moments from measurements by the Los Alamos Magnetospheric Plasma Analyzer*, LA-13566-MS, 1999.

M.F. Thomsen, final progress report for LANL LDRD project FFR20001220ER, 2001.

E.C. Whipple, Potentials of surfaces in space, *Reports on Progress in Physics, 44*, p. 1197, 1981.

E. C. Whipple, Observation of photoelectrons and secondary electrons reflected from a potential barrier in the vicinity of ATS 6, *JGR, 81*, 4, p. 715, 1976.
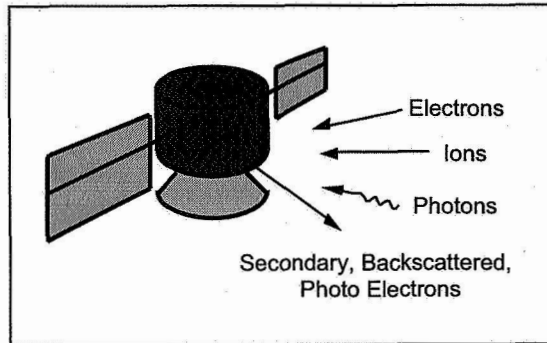
Figure 1. High negative potentials can result from the accumulation of charge on spacecraft surfaces.
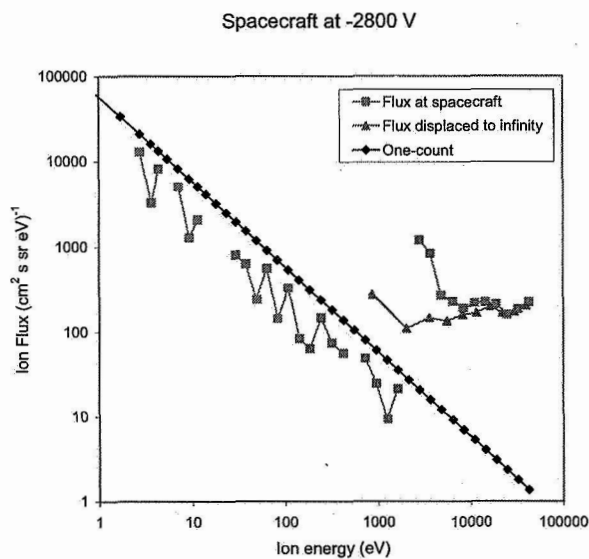
Figure 2. Ion fluxes at day 245.70276, with spacecraft at -2800. The fractional part of the day gives the time (GMT). The breaks in the "Flux at spacecraft" curve indicate zero measured flux in the energy channels not shown.

Spacecraft at -2800 V
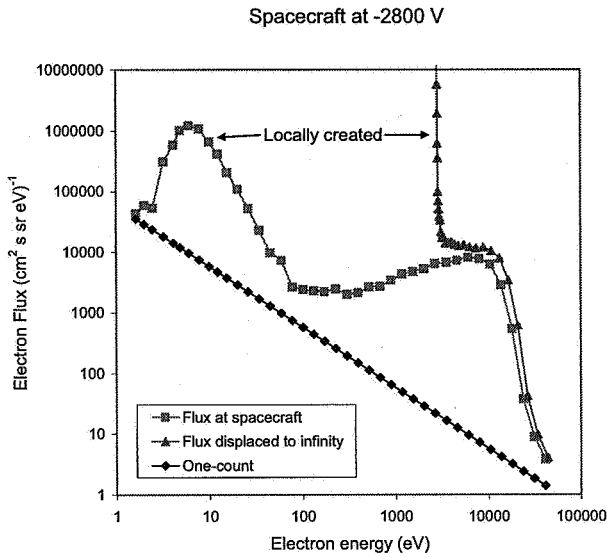
Figure 3. Electron fluxes at day 245.70276, with spacecraft at -2800 V. The fractional part of the day gives the time (GMT). The vertical line of triangles is locally created electrons.

Spacecraft at -5.4 V
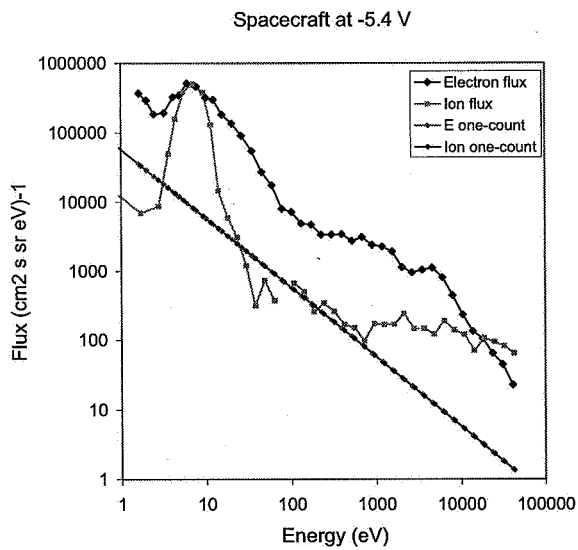
Figure 4. Measured electron and ion flux spectra at day 244.69426 with chassis at -5.4 V. The fractional part of the day gives the time (GMT).
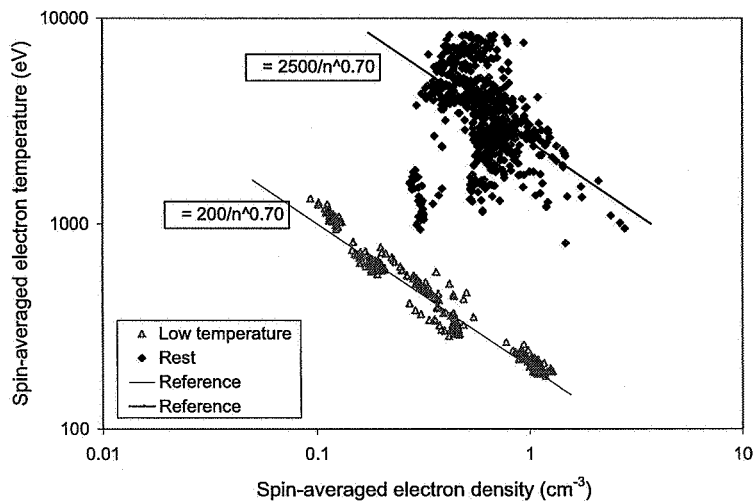
Figure 5. Temperature-density moment relationship for electrons. Data points plotted with open triangles have a value of $\theta_e n_e^{0.75} < 300 \ \mathrm{eVcm}^{-2.25}$.
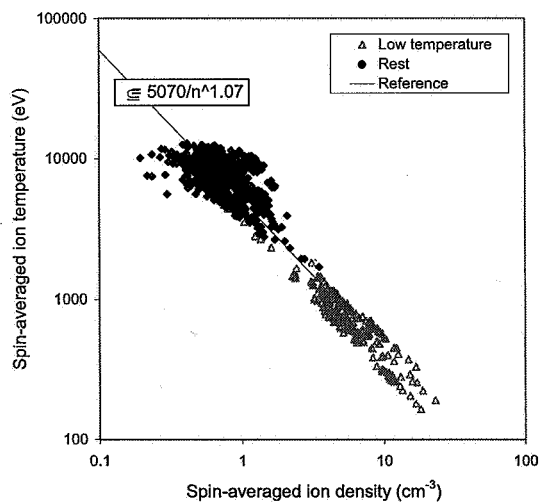
Figure 6. Temperature-density moment relationship for ions. Data points plotted with open triangles have a value of $\theta_e n_e^{0.75} < 300 \ \mathrm{eVcm}^{-2.25}$ for electrons.

26
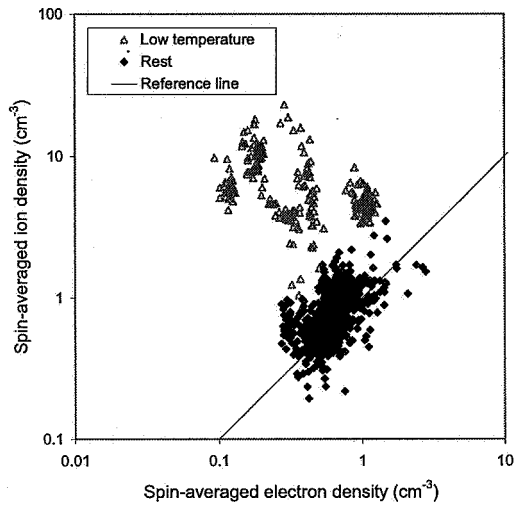
Figure 7. Ion and electron density moments are correlated and comparable. Data points plotted with open triangles have a value of $\theta_e n_e^{0.75} < 300 \text{ eVcm}^{-2.25}$ for electrons.
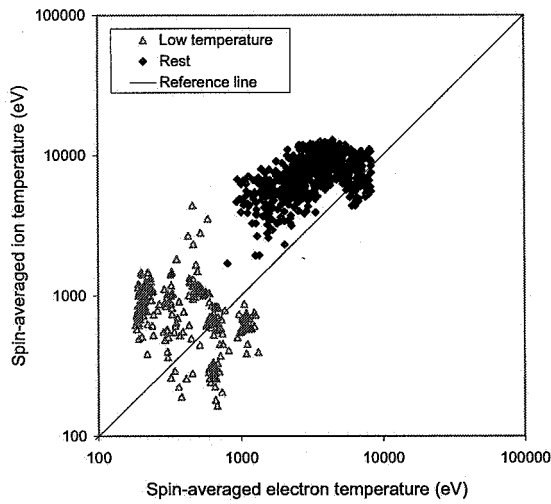
Figure 8. Ion and electron temperature moments are independent. Ion temperature moments are generally higher and vary less. Data points plotted with open triangles have a value of $\theta_e n_e^{0.75} < 300 \text{ eVcm}^{-2.25}$ for electrons.
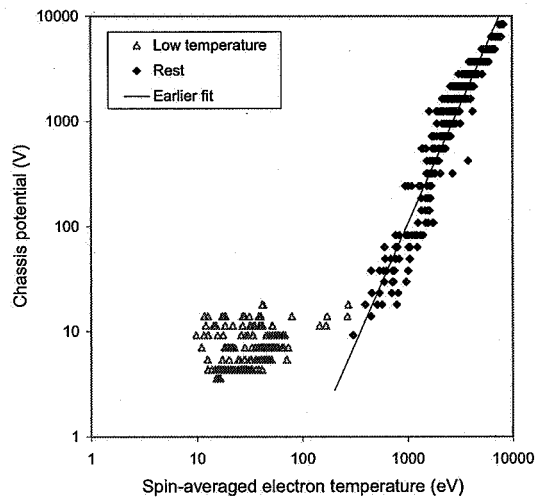
Figure 9. Measured potential as a function of a temperature moment compared with the relation $\phi = 1.74 \times 10^{-5} \left\langle \theta \right\rangle^{2.26}$. The temperature moment is computed using Equation (5). Data points plotted with open triangles have a value of $\theta_e n_e^{0.75} < 300 \ eVcm^{-2.25}$ for electrons.
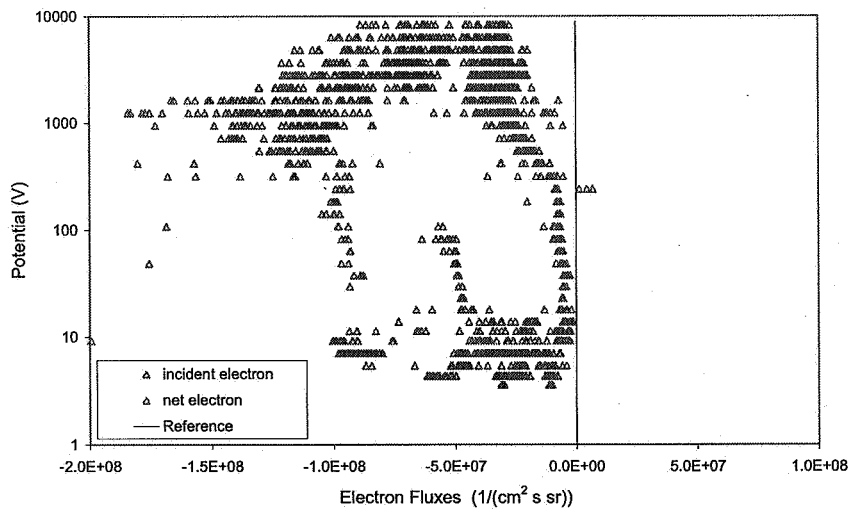
Figure 10. Electron fluxes for entire dataset. The quantity plotted is the negative of the flux.
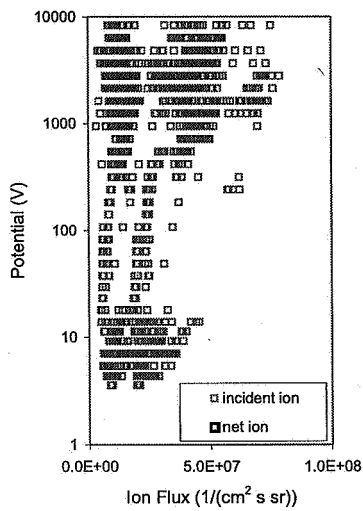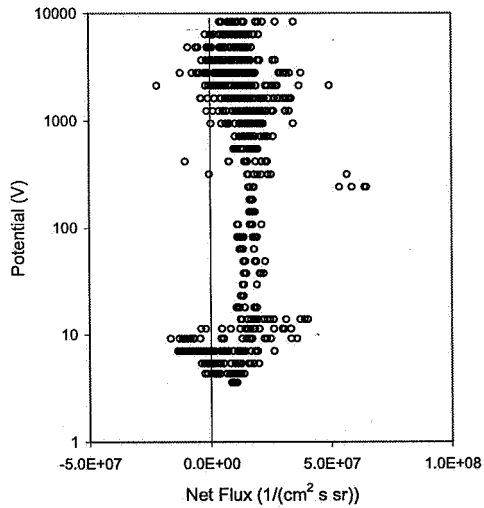
Figure 11. Ion fluxes for entire dataset.

Figure 12. Net charging flux for entire dataset. A complete flux spectrum, correct yield functions, and proper accounting for suppression of secondaries by barriers would give a value of zero for all potentials.
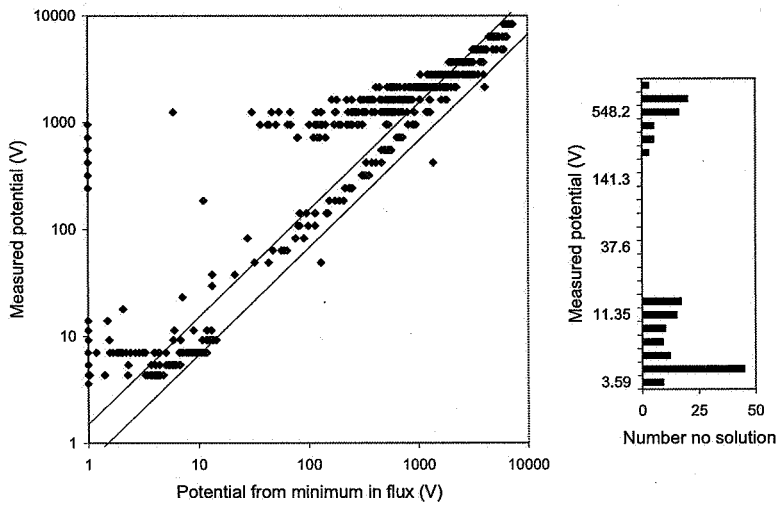
Figure 13. Measured potential as a function of the potential computed from the minimum in the net charging flux. Lines are $\phi_m = 1.5\phi'$ and $\phi_m = \phi'/1.5$.
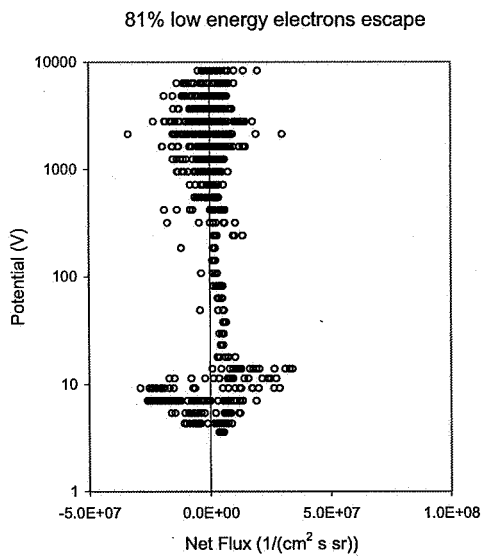

Figure 14. Net charging flux for entire dataset with 81% escape fraction.
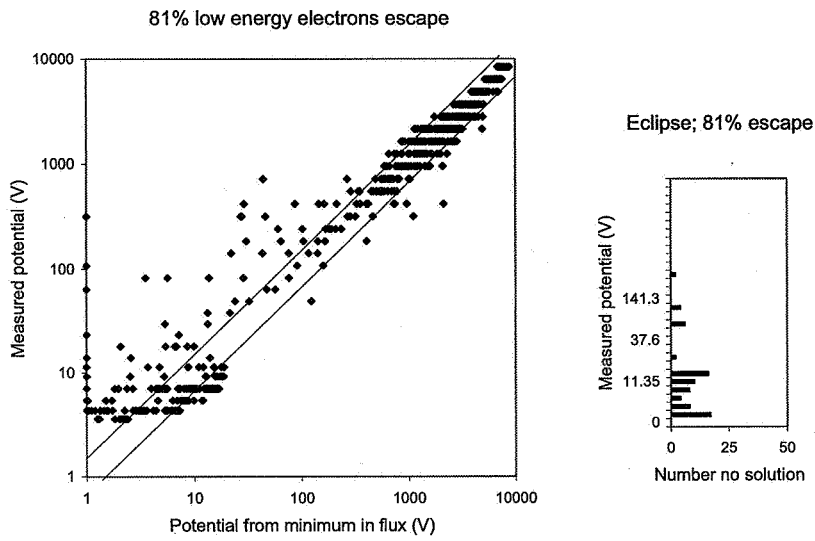
Figure 15. Measured potential as a function of the potential computed from the minimum in the net charging flux with 81% escape fraction. Lines are $\phi_m = 1.5\phi'$ and $\phi_m = \phi'/1.5$.
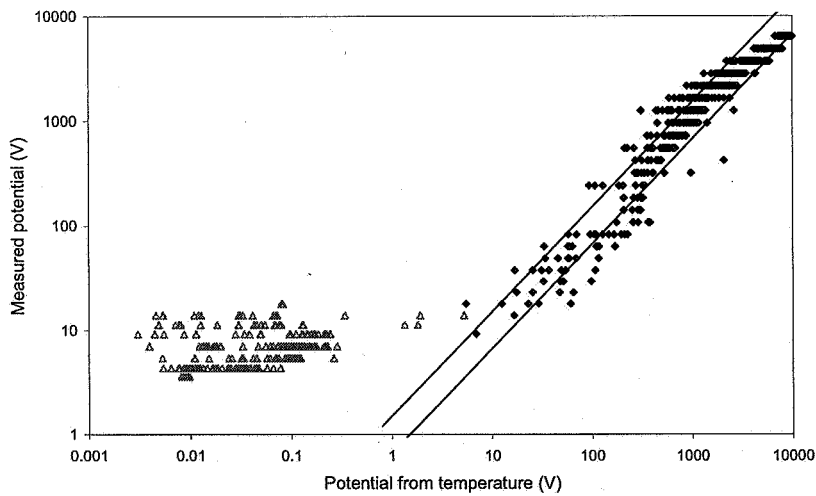

Figure 16. Measured potential as a function of $\phi = 1.74 \times 10^{-5} \langle \theta \rangle^{2.26}$. Data points plotted with open triangles have a value of $\theta_e n_e^{0.75} < 300$ eVcm$^{-2.25}$ for electrons. Lines are $\phi_m = 1.5\phi'$ and $\phi_m = \phi'/1.5$.
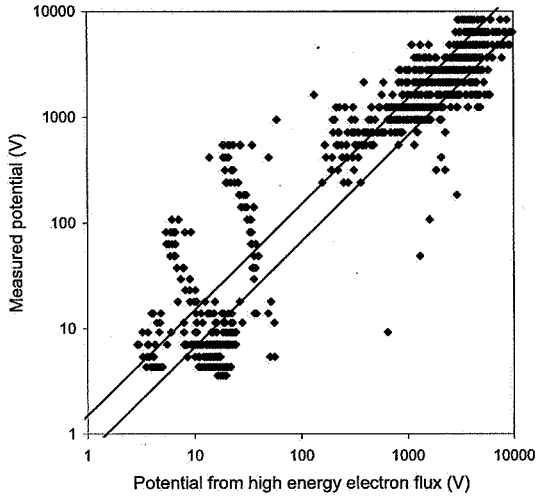
31

Figure 17. Measured potential as a function of $1.359 \times 10^{-12} \sum_{E>9123} \left(F_e \times \Delta E \right)^{2.03}$. Lines are $\phi_m = 1.5\phi'$ and $\phi_m = \phi'/1.5$.
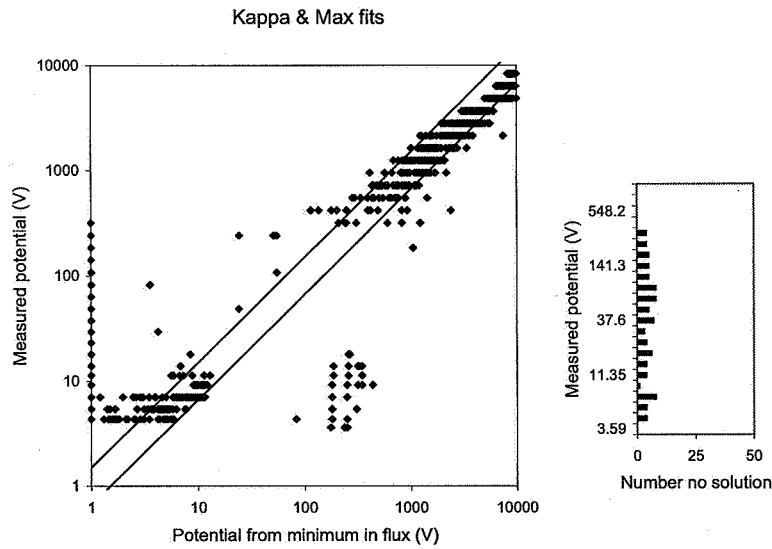

Figure 18. Measured potential computed from the minimum in the net charging flux, where the fluxes are computed from a Kappa fit to the incident electron flux and a Maxwellian fit to the incident ion flux. Lines are $\phi_m = 1.5\phi'$ and $\phi_m = \phi'/1.5$.
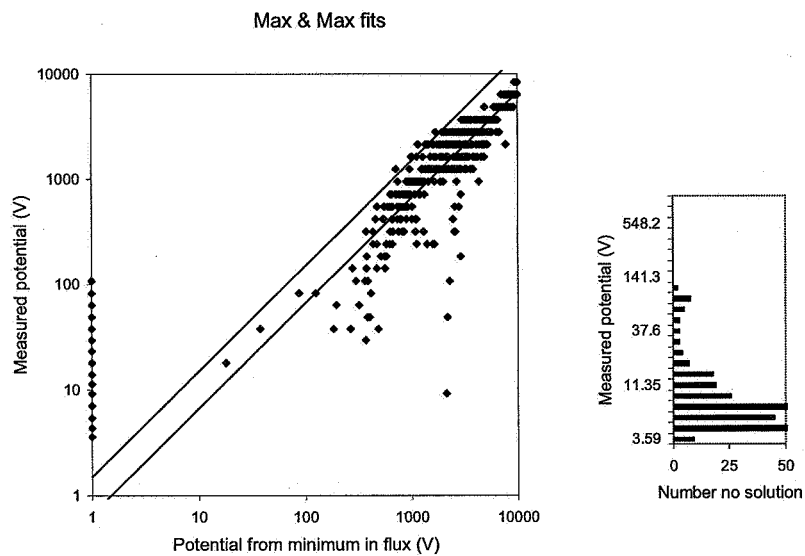
Max & Max fits

Figure 19. Measured potential as a function of the potential computed from the minimum in the net charging flux, where the fluxes are computed from Maxwellian fits to the incident electron and ion fluxes. Lines are $\phi_m = 1.5\phi'$ and $\phi_m = \phi'/1.5$.
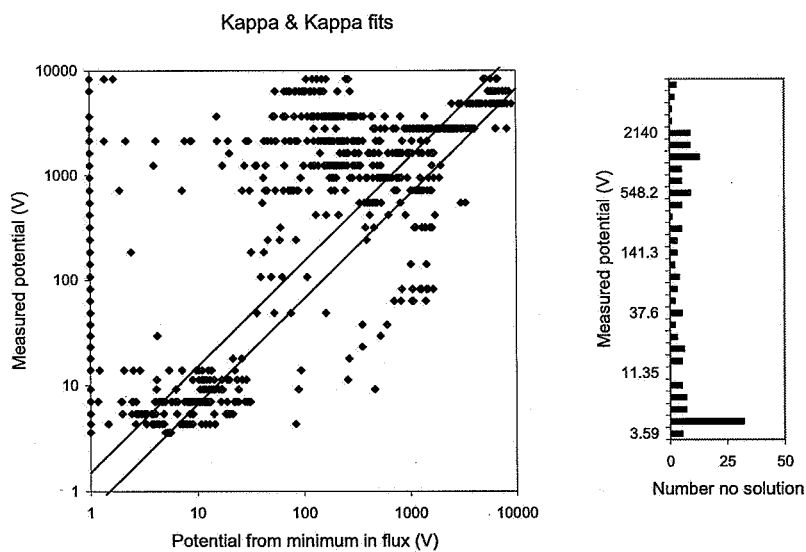

Kappa & Kappa fits

Figure 20. Measured potential as a function of the potential computed from the minimum in the net charging flux, where the fluxes are computed from Kappa fits to the incident electron and ion fluxes. Lines are $\phi_m = 1.5\phi'$ and $\phi_m = \phi'/1.5$.

33

Table 1. Average values of moments. Standard deviations in parenthesis.

	All measurements	Low temperature measurements	Rest measurements
Electron density (cm^{-3})	0.6 (0.31)	0.51 (0.39)	0.64 (0.26)
Ion density (cm^{-3})	2.4 (3.1)	6.3 (3.3)	0.81 (0.36)
Electron temperature (eV)	2700 (2100)	490 (290)	3600 (1700)
Ion temperature (eV)	5600 (3700)	800 (430)	7700 (2300)

Table 2. Quality of potential predictions made from various fits to measured incident fluxes.

Electron fit	Ion fit	Number with no match	Average error	Number within factor of 1.5	Number within factor of 3
Maxwellian	Maxwellian	338	0.37	384	599
Maxwellian	Double Maxwellian	307	0.479	322	527
Maxwellian	Kappa	263	0.478	187	344
Double Maxwellian	Maxwellian	239	0.642	484	654
Double Maxwellian	Double Maxwellian	257	0.707	300	597
Double Maxwellian	Kappa	251	0.1535	182	375
Kappa	Maxwellian	102	0.362	634	774
Kappa	Double Maxwellian	134	0.36	459	712
Kappa	Kappa	165	0.112	230	457

Table 3. Comparison of the accuracy of potential predictions from the fits when the flux integrals are done using only those energy channels used to create the fit and when the flux integrals include all energy channels and extend from 1 eV to 100 keV.

Electron fit	Ion fit	Energy channels summed	Number with no match	Average error	Number within factor of 1.5
Maxwellian	Maxwellian	1 to 100 keV	338	0.37	384
Maxwellian	Maxwellian	Same as data	342	0.84	336
Double Maxwellian	Double Maxwellian	1 to 100 keV	257	0.707	300
Double Maxwellian	Double Maxwellian	Same as data	133	0.778	494
Kappa	Maxwellian	1 to 100 keV	102	0.362	634
Kappa	Maxwellian	Same as data	106	0.469	665
Kappa	Kappa	1 to 100 keV	165	0.112	230
Kappa	Kappa	Same as data	70	0.177	298